Spin injection in the doped bad metal $SrTiO_3$

Patrizio Graziosi,[1,*] Ilaria Bergenti,[1] Lorenzo Vistoli,[1] Fabio Galassi,[1] Marco Calbucci,[1] Alberto Riminucci,[1] Francesco Borgatti,[1] Donald A. MacLaren,[2] Kerry J. O'Shea,[2] Giovanni Vinai,[3] Piero Torelli,[3] Giancarlo Panaccione,[3] Viktor Kabanov,[4] and Valentin Alek Dediu[1,†]

[1]*Istituto per lo studio dei Materiali Nanostrutturati CNR-ISMN, via Gobetti 101, 40129 Bologna, Italy*
[2]*School of Physics and Astronomy (SUPA), University of Glasgow, Glasgow G12 8QQ, United Kingdom*
[3]*Laboratorio TASC, IOM-CNR, S.S. 14km. 163.5, Basovizza, I-34149 Trieste, Italy*
[4]*JSI Jožef Stefan Institute, Jamova cesta 39, 1000 Ljubljana, Slovenia*

(Received 7 November 2022; revised 30 April 2023; accepted 14 June 2023; published 10 August 2023)

In this paper, we demonstrate the capability to establish spin-polarized currents in doped $SrTiO_3$ (STO). The results are based on the study of charge and spin transport in STO layers doped by the reversible electromigration of oxygen atoms in resistive-switching $La_{0.7}Sr_{0.3}MnO_3/STO/Co$ vertical stacks. The formation of oxygen vacancies inside STO results in a metallic conductivity at temperatures <200–250 K, above which a transition to an insulatinglike behavior is detected. A detailed theoretical analysis shows that the behavior of the metallic phase in our samples corresponds to the well-known state of the thermodynamically doped STO featuring the so-called *bad metal* behavior. Thus, our findings introduce this class of unconventional materials as valuable candidates for innovative spintronic devices.

DOI: 10.1103/PhysRevResearch.5.033096

I. INTRODUCTION

The importance of quantum materials lies in their unique properties, which offer promising applications in the fields of energy, magnetism, and electronic devices, with a profound impact on quantum technologies [1,2]. Among these, the so-called *bad metals* have been widely investigated for their superconducting, magnetic, Mott transition, and other effects [1,3–7]. Bad metals are strongly correlated materials with metallic behavior. The resistivity increases with temperature, associated with a very high resistivity value, above the maximum metallicity criterion [8–10]. In terms of charge transport, they are characterized by an unphysically low mean free path, of the order of the unit cell, which makes the suitability of a semiclassical picture questionable. Many bad metals feature a linear dependence of the resistivity over temperature, which is often taken as their main imprint [10,11], even though some materials, among which doped $SrTiO_3$ (STO) bad metal, can be characterized by their quadratic or higher temperature dependence of the resistivity [10]. Bad metals are typically complex oxides with cooperative effects emerging from the interplay between different types of order, such as charge, spin, orbital, and lattice. This results in a variety of electronic properties promoting them as promising quantum materials [3].

Oxygen-vacancy-doped n-STO has recently been identified as a clear case of bad metallicity [10,12]. Its resistivity features a complicated temperature behavior showing a standard T^2 law at low temperatures [10,13,14], cubic at $\sim$100 K, where the mean free path of carriers decreases below their wavelength while, further, it falls below the interatomic distance at/above room temperatures. Notably, both metallic and insulating regimes can be found in doped STO, according to doping levels [15], and both are appealing for applications. The metallic one is an unusual metal whose properties have yet to be better understood. The insulating phase is the strongest dielectric and is characterized by colossal spin-orbit coupling [16]. Currently, there is a continuously growing interest in the application of STO in spintronics, with a particular interest for spin-orbit torque applications [17].

Magnetoresistive studies are actively employed to study the bad metals, especially those characterized by ordered magnetic structures, like $SrRuO_3$ and others [1,18–20]. However, the possibility to establish spin-polarized currents has not been investigated.

Here, we prove unambiguously that spin-polarized transport can be achieved in STO bad metal. We investigated *ad hoc* tailored electronic devices based on ferromagnetic manganite and Co spin-polarized electrodes and doped-STO as a transport channel. The $La_{0.7}Sr_{0.3}MnO_3$ (LSMO) manganite and cobalt represent a well-established pair of spintronic electrodes [21–23], providing efficient means for the analysis of the spintronic properties of STO. Oxygen vacancy doping of STO was obtained by the reversible electromigration of oxygen atoms in LSMO/STO/Co vertical devices. Our findings enlarge the playground of bad-metal applications as quantum

*patrizio.graziosi@cnr.it
†valentin.dediu@cnr.it

Published by the American Physical Society under the terms of the Creative Commons Attribution 4.0 International license. Further distribution of this work must maintain attribution to the author(s) and the published article's title, journal citation, and DOI.

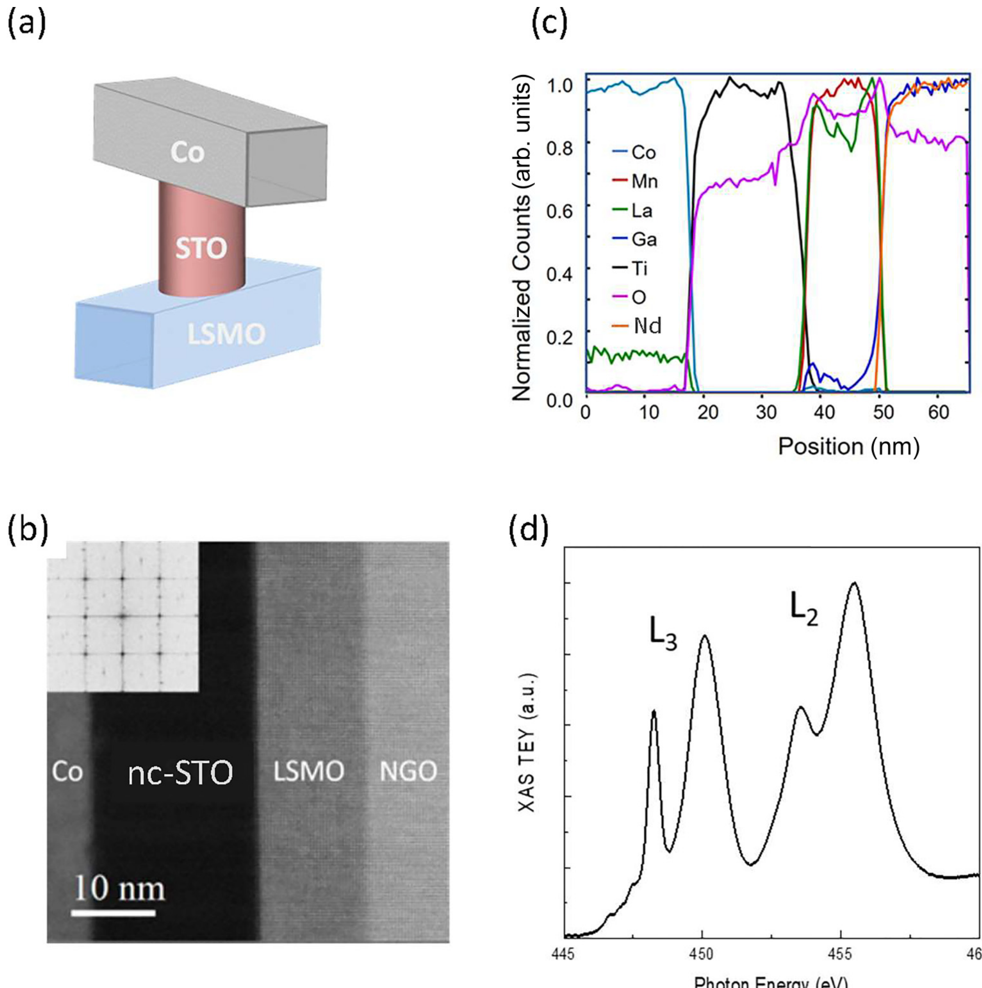

FIG. 1. (a) Device structure. (b) High-resolution transmission electron microscopy (HR-TEM) cross-section image. The inset shows the Fourier transform corresponding to LSMO on NGO. (c) Compositional analysis by electron energy loss spectrometer (EELS) of the section in (b). (d) X-ray absorption spectroscopy (XAS) line shape for Ti $L_{2,3}$ edge of nc-STO.

materials and establish a link with neuromorphic computing via the interplay between spin transport and tunable resistivity.

II. METHODS

Charge and spin transport in doped STO has been investigated in four-terminal crossbar devices using LSMO and cobalt electrodes. The devices were fabricated by shadow masking techniques on single-crystal $NdGaO_3$ (110) substrates [NGO, Fig. 1(a)], allowing us to obtain $500 \times 500\ \mu m$ junctions. The oxide components of the devices (bottom LSMO contact and STO layer) were fabricated by channel spark ablation from stoichiometric targets [24]. Polycrystalline STO layers with 10–25 nm thicknesses were deposited at 450 °C in O_2 atmosphere on 15-nm-thick LSMO following the procedure described in Refs. [24,25]. The Co top electrode (10–50 nm thick) was deposited by electron beam deposition at room temperature. The doping of STO was performed by electromigration of oxygen atoms in vertical devices, based on the well-established resistance bistability effects in STO [26].

Magnetic characterization of electrodes was carried out by magneto-optical Kerr effect (MOKE) at room temperature in a longitudinal configuration with $\lambda_{exc} = 632.8$ nm. Transmission electron microscopy was performed on a JEOL ARM cFEG instrument equipped with a Gatan Quantum electron energy loss spectrometer (EELS). Cross-sectional samples were prepared using standard protocols on an FEI Nova Focused Ion Beam instrument.

The x-ray absorption spectroscopy (XAS) spectrum was taken at the APE-HE beamline of the Elettra synchrotron radiation facility in Trieste [27] in total electron yield (TEY) mode on a sample holder that allows current-voltage (I-V) characterization in a two-point configuration directly within the analysis chamber [28]. The sampling depth in TEY measurements is typically ∼8–10 nm and allows us to investigate deep regions within a working device and to study the effects of the resistive switching on the top electrode and the underlying STO layer. To eliminate the oxidation and contamination of the air-exposed side of the Co electrode, all samples were mildly Ar^+ sputtered ($E = 500$ eV for 30 min) in the preparation chamber before spectroscopic investigations. Electrical

characterization was carried out using a Keithley 236 Source Measure Unit and with samples held in an external magnetic field of up to 1 T. The measurements were performed with the Co electrode grounded.

III. RESULTS

A. Structural characterization

The investigated devices are characterized by sharp and well-defined interfaces between the electrodes and the STO, as demonstrated by scanning transmission electron microscopy (STEM) cross-section investigation, Fig. 1(b). Atomic columns in the NGO substrates and LSMO electrode are clearly resolved, and their epitaxial relationship is apparent, as evidenced by the inset in Fig. 1(b), showing the Fourier transform dominated by a single square pattern of spots deriving from both layers. In contrast, the STO and Co show little internal structure or ordering in agreement with their polycrystalline nature.

The compositional analysis [Fig. 1(c)], taken on the full sample section, shows that the oxygen signal in the STO layer is lower than that of the titanium one, indicating the presence of oxygen vacancies, while the high contrast of the STO layer indicates some deficiency in heavier elements like Sr. The XAS line shape for the Ti $L_{2,3}$ edge of the STO layer [Fig. 1(d)] denotes a sequence of four main bands, corresponding to Ti^{4+} in an octahedral crystal field with alternating t_{2g} and e_g symmetry [29]. The signal fits the standard STO contribution [30], whereas some broadening of the bands could either be attributed to a reduction of Ti or/and changes in the coordination of the Ti^{4+} cations [31]. We cannot also rule out the possible presence of TiO_2 [32] inclusions, which would not contradict both compositional analysis and high contrast detected by TEM. Thus, the STO layer appears to be nanocrystalline, with very small, randomly oriented, crystalline grains, and having oxygen vacancies and possible segregations of the TiO_2 phase (for example, at the grain boundaries).

B. Transport properties

We focus now on the charge transport behavior across STO. The pristine STO layers are insulating with a thermally activated Arrhenius type temperature dependence [$\exp(-E_a/k_BT)$] of the resistance $R(T)$, ranging from 10^7 to 10^9 Ω at 100 mV measuring voltages. We call this the initial resistance state (IRS) and report it in Fig. 2. The Arrhenius fit reveals activation energies $E_a < 0.1$ eV, lower than typical activation energies (∼0.4 eV) of oxygen vacancies in STO and other oxide perovskites [33–35]. The IRS clearly corresponds to an unintentionally doped regime, governed possibly by various defects and impurities, and its description and understanding are beyond the scope of this paper. The low activation energies may correspond to the nature of specific doping species and indicate that the low measuring voltage does not induce nonlinear effects related to the creation/moving of defects during the transport measurements.

Next, we perform the doping of the STO layer with oxygen vacancies by employing the well-known electromigration effects, guiding the resistive switching in this material [36–38]. Figure 3 shows various I-V curves at 100 K and indicates that,

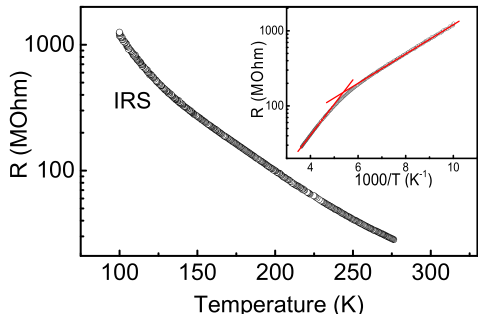

FIG. 2. Temperature dependence of the resistance of the initial resistance state (IRS) before electrically induced doping, and the fits with Arrhenius' law in the inset. Two regimes are detected, corresponding to activation energies of 0.04 eV (left-hand side, lower temperature) and 0.08 eV (right-hand side, higher temperature), with a crossover at ∼170 K.

>+5 V, the resistance is irreversibly modified from 10^9 Ω to 10^4–10^5 Ω for a selected sample with 15-nm-thick STO, where the sign of the voltage is taken with respect to the grounded Co electrode. After this initial forming process, the resistance can be tuned by programming voltages in a multimodal resistive switching behavior (Fig. 3). The resistance tuning follows a bipolar regime, i.e., the resistance decreases at positive programming biases and is restored at negative biases. In the framework of electromigration of oxygen atoms in the STO layer, the positive bias moves the oxygen species from STO to manganite, enhancing the concentration of oxygen vacancies and hence the system conductivity, while at negative biases, the oxygen flow is reversed, reducing partly the carrier concentration. On the other hand, the manganite in the configuration La(0.7)Sr(0.3) is close to the stability region of the phase diagram, and small oxygen variations do not induce measurable variations of electrical and magnetic properties. The samples can thus be reversibly switched from low-resistance states (LRSs) to high-resistance states (HRSs)

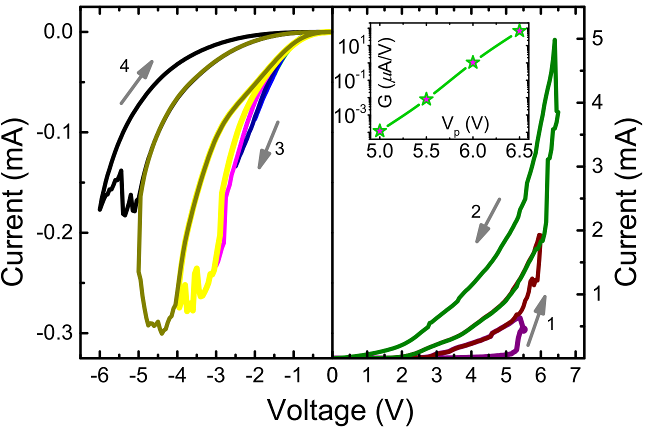

FIG. 3. Current-voltage characteristic showing resistive multistability behavior. The initial resistance state (IRS) is switched at threshold voltage $V_{th} = 4.8$ V to low-resistance state (LRS). The state is stable until the application of a negative bias (−2.5 V), which puts the device in high-resistance state (HRS). Blue arrows indicate the sweep direction. Inset: Zero-bias conductance vs programming bias.

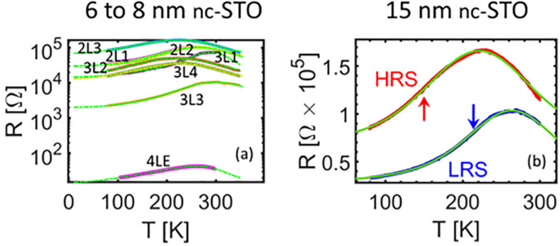

FIG. 4. Resistance as a function of temperature after the application of the forming pulse: (a) a set of samples from two separate batches with, as electrodes, 15 nm LSMO (250 Ω − 1 KΩ across the temperature range, not shown) and 10 nm Co (450–550 Ω across the temperature range, not shown), and STO interlayer of thickness 7 ± 1 nm, as evaluated by combining growth calibration and post-process characterization. The curves are from three different devices in different (low) resistance states, resulting from different programming (doping) bias. The curves are labeled as dLn (device, low resistance, number of the curve). The label E is for extremely low resistance. (b) The sample with 15-nm-thick STO, employed further in quantitative evaluation of bad metal parameters. The arrows highlight the flexus point where the curvature changes from positive to negative; we consider the part of the $R(T)$ having a positive curvature metallic, left-hand side of the arrow.

and back, by positive or negative programming voltages, respectively. We also observe an exponential enhancement of zero-bias conductivity vs positive applied programming voltages V_p, where V_p is defined as the highest voltage achieved in each resistive loop (inset in Fig. 3), in good agreement with models for the field-induced migration of vacancies [37]. Indeed, our doping proceeds by electromigration of oxygen vacancies from the electrode, strongly depending on the diffusion of oxygen at the interface. The activation energy for the migration of oxygen vacancies in oxides decreases linearly with the applied electric field so that the probability of diffusion of oxygen vacancies through the interface with the electrode becomes exponential with V_p. Moreover, our electric field is on the order of 10^6 V/cm, in good agreement with Ref. [37]. This indicates that we are varying the density of oxygen vacancies in the STO layer by means of the applied electric field. This effect is notoriously of filamentary type, promoting highly conducting nano- and microchannels inside an undoped matrix [39]. Below, we compare our results with those from thermodynamically doped single crystals [10].

Having established the technology for the control of the doping levels of STO-based vertical stacks, we now investigate the physics of the electrical transport in our doped samples by analyzing the resistance at low, nondisturbing, reading voltages $V_r = 100\,\text{mV} \ll V_p$.

Figure 4 shows the temperature dependence of the resistance for various doped samples, together with a fitting function depicted in dash-dot green lines. The resistance exhibits a metalliclike behavior ($dR/dT > 0$) at low temperatures, changing to insulating comportment ($dR/dT < 0$) above the metal-insulator transition (MIT). The presence of both metallic and insulating regimes on the same sample is by itself unusual, even though a transition from fully metallic to fully insulating $R(T)$ curves at lower doping levels can be routinely observed for doped STO [13,15,40]. We cannot

TABLE I. Fitting parameters for the fitting line in Fig. 3(a), R_{square} agreements are 0.9997 and 0.9972 for LRS and HRS, respectively.

Parameter	LRS	HRS
R_0 (kΩ)	30	73
α	1.65	1.55
E_a (eV)	0.28	0.25
T_p (K)	285	260
T_w (K)	117	150

exclude the achievement of a specific intermediate doping level established by the electromigration, which can maintain both conducting branches. Nevertheless, we believe that the transition is mainly induced by local inhomogeneities of the doping concentrations caused by the coexistence of mixed metallic and insulating phases and discuss this in more detail below.

Mathematically, the resistance of similar samples showing a temperature-induced MIT can be described through the expression:

$$R(T) \sim \Re_M^{\delta} \Re_I^{1-\delta}, \tag{1}$$

where $\Re_M$ describes the metallic part with a power law $\Re_M \sim T^{\alpha}$, already assessed for metallic thermodynamically doped STO samples [10], whereas $\Re_I$ accounts for the insulating phase as an Arrhenius law $\Re_I = \exp(E_a/k_B T)$. The volume fraction of the metallic phase is described by the error function $\delta(T) = 0.5 - 0.5\text{erf}(\frac{T - T_{\text{MIT}}}{T_w})$ [41–43]. Here, T_{MIT} is the MIT temperature, which does not necessarily coincide with the peak in $R(T)$, and T_w is the width of the MIT. The fitting function, in addition to offering a general description, is widely used in the Discussion section.

In Fig. 4, we keep, in the left-hand-side panel, several samples with STO thickness in the 6–8 nm interval and, in the right-hand-side panel, one 15 nm sample with two doping levels, established by 5 and 5.5 V programming biases. Given the similarities between various samples and for the sake of simplicity, we focus mainly on this sample, and its two states are called hereafter HRS (red dots) and LRS (blue dots), respectively. The set of parameters extracted from best fits for these LRS and HRS are reported in Table I.

Ultimately, we take advantage of the high spin polarization of the employed electrodes and investigate now the possibility to establish spin-polarized currents in our devices, moving the polarized carriers across the doped STO layer. We perform this in the standard spin-valve approach by comparing the (magneto)resistance for parallel and antiparallel orientations of the respective magnetizations. STO has frequently been used as a tunnel barrier in magnetic tunnel junctions (MTJs) with LSMO and Co spin-polarized electrodes, having pioneered the detection of the interfacial spin filtering effects [44]. As indicated by the transport analysis for both LRS and HRS, and as shown in more detail below, we have clear evidence for carrier transport inside the STO layer. The detection of magnetoresistance (MR) would indicate thus in a straightforward way the establishment of spin-polarized currents in the framework of the bad-metal transport mechanism.

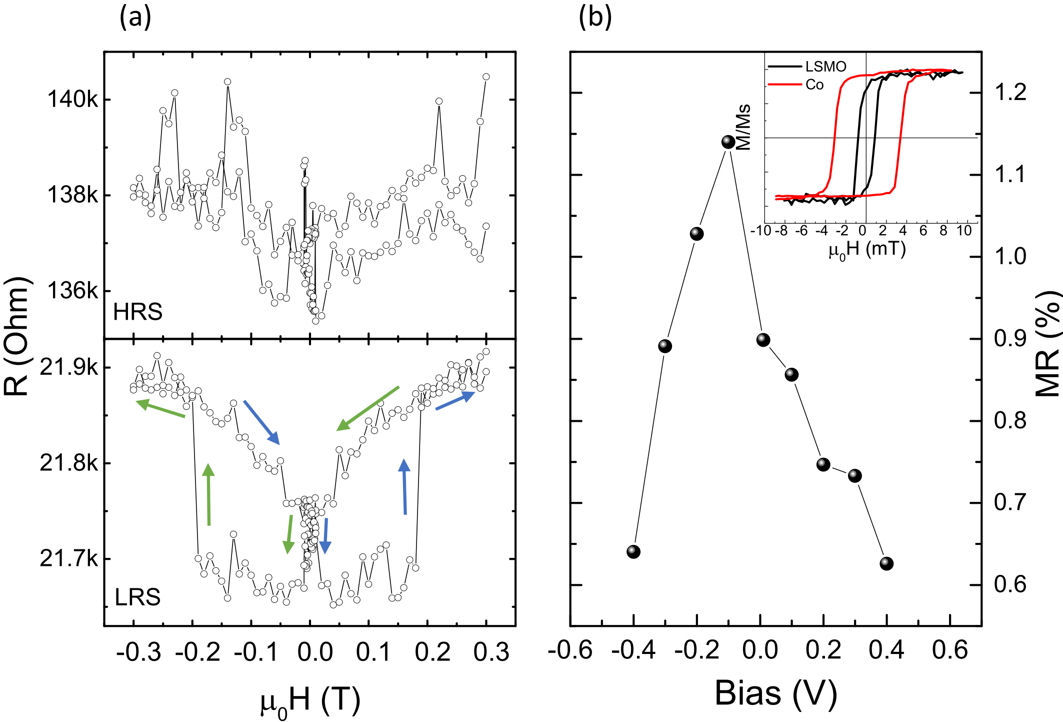

FIG. 5. (a) Resistance curves as a function of applied external field measured at 100 K in the high-resistance state (HRS; upper panel) and the low-resistance state (LRS; lower panel). (b) Dependence of the negative magnetoresistance (MR) ratio on the applied bias voltage in the LRS. The inset shows the hysteresis cycles measured at room temperature by magneto-optic Kerr effect (MOKE) for the LSMO (black line) and Co (red line) layers.

Figure 5(a) shows the results of MR measurements for the two LRS and HRS conducting cases for the 15 nm nc-STO devices. MR was performed at 100 K, keeping the measuring temperature well below the Curie point of LSMO (300 K for our thicknesses) and applying the external magnetic field in the film plane. As for the $R(T)$ curves, the applied voltage ($V_r = 0.1$ V) is kept well below the programming values, thus avoiding modifications of the oxygen vacancy configuration.

The LRS is characterized by a sharp spin valve effect of $\sim$1 % of resistance variation between parallel and antiparallel electrode orientations. The enhancement of the resistance on the same sample by the programming bias (HRS case) significantly decreases the MR down to the level of the measurement noise ($\sim$0.5 %) or lower. Note that most of the samples in Fig. 4(a) show MR like our prototypical sample. Then the MR was zero in all IRS devices.

Note that the spin valve effect in LRS is inverted with respect to projected higher resistance for the antiparallel configuration. Analogous behavior is notoriously characteristic for tunneling devices with the combination of the same materials, where the Co-Ti hybridization strongly modifies and inverts the spin polarization at the Co/STO interface [21,45].

Another analogy with the LSMO/STO/Co MTJ device [21] is represented by the larger switching fields of the Co electrode with respect to the measured bulk coercive field—the inset in Fig. 4(b) shows the hysteresis loops for both electrodes. While known for long time [21], such deviations in the device coercive fields have recently been explained based on interfacial hybridization [46], able to modify the magnetic anisotropy by more than one order of magnitude [47,48].

Finally, Fig. 5(b) shows the dependence of the MR on the applied reading voltage, where a decay distinctive for both MTJ and charge/spin transport devices is typically due to the specific band structure of electrodes and established interface states [49].

IV. ANALYSIS AND DISCUSSION

A. Charge transport

Now we move toward a more accurate description of the charge transport data. Since the electromigration control of the doping in crossbar devices does not allow us to extract the sample resistivity, we proceed by reporting the observed trends rather than absolute values. It has been shown that, for a wide range of doping concentrations (exceeding 10^{17} cm^{-3}), the $R(T)$ curves of metallic STO can be well described by a power law, involving a *universal concentration-independent* parameter $\alpha(T)$:

$$R(T) = R_0 + AT^{\alpha}. \tag{2}$$

This exponent α characterizes the metallic state and is typically computed by using the logarithmic derivative of the transport data and by considering it as a constant $\alpha \neq \alpha(T)$ [10]:

$$\tilde{\alpha} = \frac{d\ln(R - R_0)}{d\ln T}. \tag{3}$$

For this data representation, we consider only the metallic parts of $R(T)$ characterized by a positive curvature, as highlighted by the arrows in Fig. 4(b). We keep thus below the deviations induced by the MIT. We use the notation $\tilde{\alpha}$ because

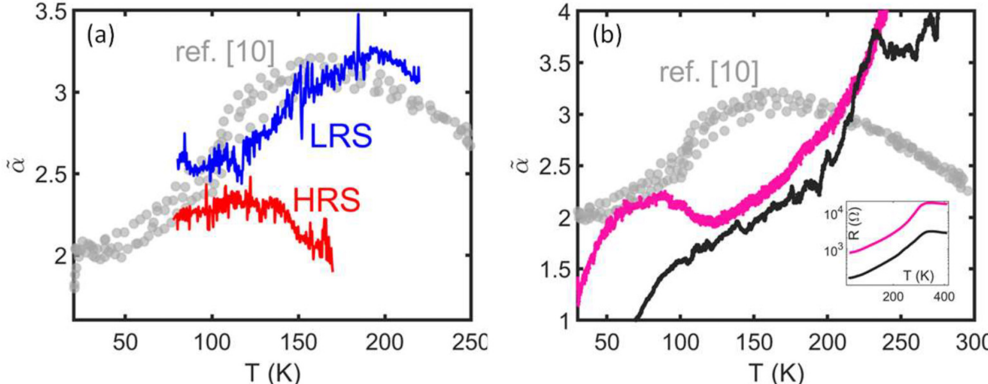

FIG. 6. (a) $\tilde{\alpha}(T) = \frac{d\ln(R-R_0)}{d\ln T}$ values for nc-STO, and for comparison, the values for single-crystal STO doped with oxygen vacancies [10], depicted with gray dots, computed using Eq. (3). (b) $\tilde{\alpha}(T)$ of LSMO thin films of thickness 9 and 13 nm; like the used electrodes, the corresponding $R(T)$ measured with four-probe van der Paw technique [24] are reported in the inset. It appears clear that the device behavior shown in (a) does not depend on the LSMO electrodes.

the proper α, used in the $\sim T^\alpha$ law, is indeed a function of temperature rather than a constant and should be derived as well.

The calculation of $\tilde{\alpha}$ as in Eq. (3) allows an immediate comparison with the literature data on single-crystal STO. We derived R_0 from the fits in Fig. 4(b) and report the $\tilde{\alpha}$ values for our nc-STO in Fig. 6(a), blue line for LRS and red line for HRS, for the 15 nm nc-STO devices. Here, we compare our data with the literature, gray dots [10]. Our points are on track with single-crystal STO, demonstrating that we are measuring transport through STO and that our nc-STO has transport features comparable with the single-crystal STO doped by thermodynamic processes [10]. While the LRS is clearly very similar to the single-crystal STO data, the HRS appears somehow different. However, the metallic region for the HRS is very limited, and this can impact the analysis.

We strengthen this conclusion by performing the same transport analysis for epitaxial LSMO thin films, which are complex perovskite oxides, like STO, and are used as bottom electrodes. We depict the case of LSMO in Fig. 6(b), where the $\tilde{\alpha}$ values for two LSMO films of 9 and 13 nm thickness are compared with the reference STO data; the $R(T)$ data are shown in the inset. It appears that the $\tilde{\alpha}$ exponent of the LSMO contact is radically different from both thermodynamically doped STO and from our devices, which validates that our findings are not artifacts induced by LSMO [50] but come from transport in the nanocrystalline STO. Additionally, this type of artifact appears when the device resistance is similar or lower than the contact resistance [50], whereas the resistance of our LSMO electrodes is an order of magnitude lower than the devices.

We now present a way to define α for the metallic-behavior interval by including its temperature dependence. Indeed, if we were to perform a logarithmic derivative of Eq. (2), we would obtain

$$\frac{d\ln(R-R_0)}{d\ln T} = \alpha + \ln T\frac{d\alpha}{d\ln T}, \quad (4)$$

where the second term at the left-hand side of Eq. (4), $\ln T\frac{d\alpha}{d\ln T}$, was generally neglected [10]. Because our measurements are limited to liquid nitrogen temperature and we lack experimental knowledge about both R_0 and A terms in Eq. (2), we accurately redefine α by means of a linear temperature derivative and then a logarithmic derivative to get rid of both the unknown R_0 and A, and in each passage, we hold $\alpha = \alpha(T)$. We obtain the following differential equation:

$$\frac{d\ln\left(\frac{dR}{dT}\right)}{d\ln T} = \alpha - 1 + \frac{d\alpha}{d\ln T}\ln T + \frac{d\ln\alpha}{d\ln T} + \frac{d\ln\frac{d\alpha}{dT}}{d\ln T}. \quad (5)$$

Equation (5) can be recast as

$$y + \frac{dy}{dx}x\ln x + \frac{d\ln y}{dx}x + \frac{d\ln\frac{dy}{dx}}{dx}x = 1 + f, \quad (6)$$

where $y = \alpha$, $x = T$, and $f = \frac{d\ln(\frac{dR}{dT})}{d\ln T}$ is a function that depends only on the experimental data. We have applied the chain rule $\frac{dy}{d\ln x} = \frac{dy}{dx}\frac{1}{d\ln x/dx} = \frac{dy}{dx}x$. Equation (6) can be solved provided initial conditions for y and y' [51].

After we have obtained $\alpha(T)$ using Eq. (6), we can compute $\alpha + \ln T\frac{d\alpha}{d\ln T}$, which allows us to directly compare back with literature data after Eqs. (3) and (4): $\alpha + \ln T\frac{d\alpha}{d\ln T} = \frac{d\ln(R-R_0)}{d\ln T} = \tilde{\alpha}$. In circular feedback, we consider valid initial conditions the ones which enable us to agree as much as possible with the literature data [10], gray dots in Fig. 6(a), or with our data, blue and red lines in Fig. 6(a). These are depicted in Figs. 7(a) and 7(d), respectively, with LRS represented by the dash-dot blue line and HRS by the dash-dot red line. In Fig. 7(a), the gray dots are the experimental data and represent the values and their spread/uncertainty, like in Fig. 6, whereas in Fig. 7(d), the lines correspond to the ones in Fig. 6(a).

We first use the fitting curves, which can be computed at any temperature, to express the function f, always limiting to the metallic part, as detailed above. These are the dash-dot lines in Fig. 7, where the blue color is for LRS and the red color is for HRS. Thanks to this step, we can extract the values for y and y' at the liquid nitrogen temperature and solve Eq. (6) again using the experimental resistances instead of the fitting curves. The obtained values of α are represented by solid lines in Figs. 7(b) and 7(e) for the cases with the initial conditions for solving Eq. (6) mapped over the literature data or our data, respectively. These can be regarded as the proper $\alpha(T)$ values in Eq. (2).

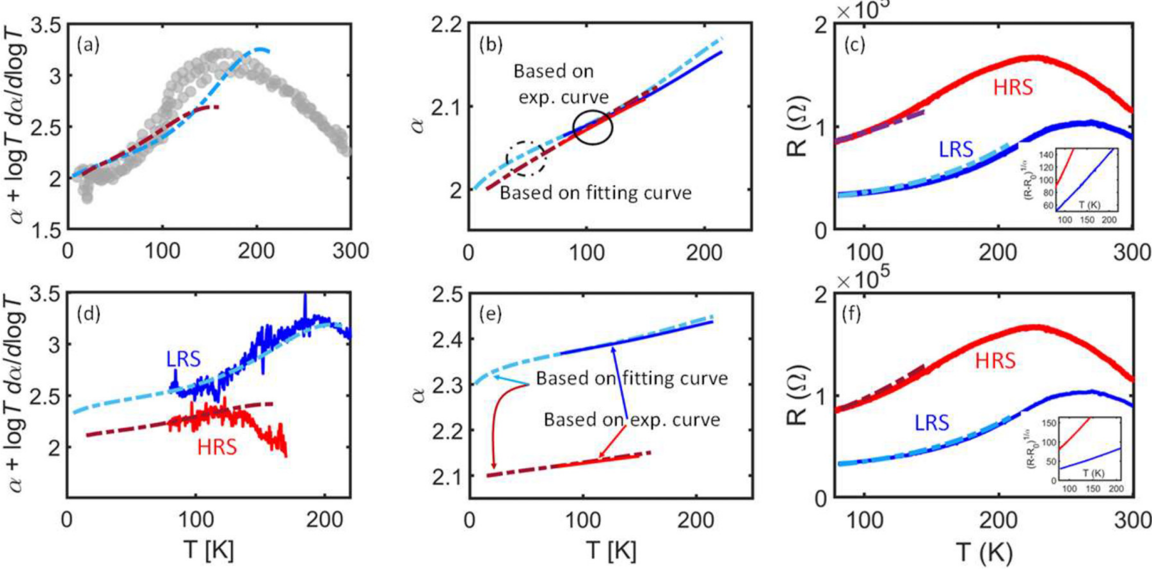

FIG. 7. (a) $\tilde{\alpha} = \alpha + \ln T \frac{d\alpha}{d \ln T}$ term computed after having solved Eq. (6), assuming initial conditions that enable us to match as much as possible the literature data for $\frac{d \ln(R-R_0)}{d \ln T}$, gray dots [10]. Blue line is for low-resistance state (LRS) and red line for high-resistance state (HRS). (b) The proper α values computed with Eq. (6) for initial conditions mapped over literature data. Dash-dot lines are for the first step, when we consider values from the $R(T)$ fit, and solid lines are for the second step, when we consider experimental points. (c) Calculation of the resistance based on the computed α values. The inset shows that $(R - R_0)^{1/\alpha}$ is linear with T. (d) Same as (a) but with the initial conditions mapped over our transport data, reported with solid lines as in Fig. 3(b). (e) The proper α values computed with Eq. (6) for initial conditions always mapped over our transport data. Dash-dot lines are for the first step, when we consider values from the $R(T)$ fit, and solid lines are for the second step, when we consider experimental points; blue for LRS, red for HRS. (f) Same as (c) but for the case when only our experimental data are used at any step of the resolution of Eq. (6).

To confirm that the obtained values are the correct value of α, we show that, by using these values, it is possible to reproduce the measured resistance. In Figs. 7(c) and 7(f), the dash-dot lines represent the computed resistance values, while the solid lines are the experimentally measured resistance. To reproduce the measured value from the extracted α, we linearize the resistance vs temperature as $(R - R_0)^{1/\alpha}$ [insets in Figs. 7(c) and 7(f)], and by fitting $(R - R_0)^{1/\alpha}$, we obtain the A value which, using Eq. (2), enables us to compute the resistance. The R^2 of the fits is > 0.995, and we underline that the value we use for R_0 is the same obtained from the initial fits, for consistency, and has not been optimized to reproduce the experimental values. Thus, we developed a convenient procedure to compute the temperature-dependent exponent of the resistance in bad metals from transport measurements.

After having clarified the conceptual picture of the transport in our devices, we go further in understanding the physical nature of the transport in our doped nc-STO. Considering that the adopted doping procedure is electrically driven, the maximum doping density should be limited by the electrical repulsion between dopants, which cannot exceed the applied electric field. We start analyzing the minimum distance between two oxygen vacancies by assuming they are punctual charges having a 2+ charge and assuming a screened Coulomb potential around them. We define such a minimum distance as the distance at which the repulsive electric field equals the programming field assumed as $F_p = 3 \times 10^6$ V/cm. The screened potential, in centimeter-gram-second (c.g.s.) system of units, is [52,53]

$$\varphi = \frac{2e}{\varepsilon_0 \varepsilon_r} \frac{1}{r} e^{-r/\lambda}, \tag{7}$$

where r is the radial distance from the vacancy, and λ is the screening length. The electric field:

$$F = -\nabla\varphi = \frac{2e}{\varepsilon_0 \varepsilon_r} \left[\frac{1}{r^2} + \frac{1}{r\lambda}\right] e^{-r/\lambda}, \tag{8}$$

is plotted in Fig. 8(a), for $\lambda = 0.1$, 1, and 10 nm, using $\varepsilon_r = 200$ (solid lines) or 20 (dash-dot) to consider the defective nature of nc-STO.

The screening length in epitaxial STO thin films is assumed to be $\sim$1 nm [54], whereas in metallic doped STO, a much longer screening length value is envisaged, of the order of 50 nm [55,56]. Since a screening length of 10 nm is nearly identical to the unscreened potential case, we take 1 nm as the order of magnitude of the distance between the oxygen vacancies to achieve a field value like the programming one, which results in a distance between the oxygen vacancies of 2 or 3 unit cells since the unit cell of STO is 0.4 nm. Thus, we can assume a cylindric filament of diameter $\sim$0.8 nm. In the case of a 10-nm-long filament, which contacts LSMO and Co, with 10 vacancies, we get a density of $\sim 2 \times 10^{21}$ cm^{-3}. Again, a vacancy inside a sphere of diameter 1 nm gives a density of $\sim 2 \times 10^{21}$ cm^{-3}. This carrier density maps very well with the ones indicated by Huang *et al.* [57] in a recent work about the metallicity in STO bulk and thin films. We

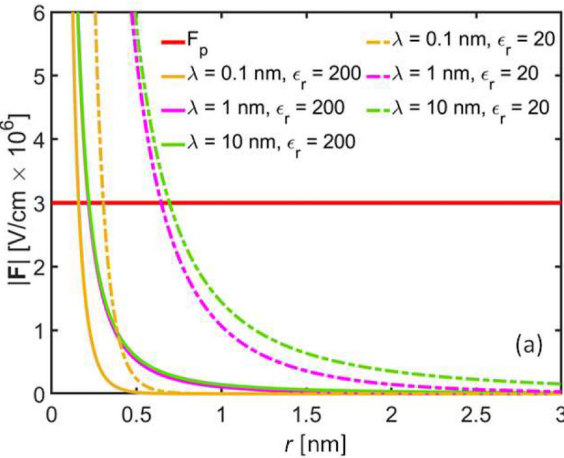

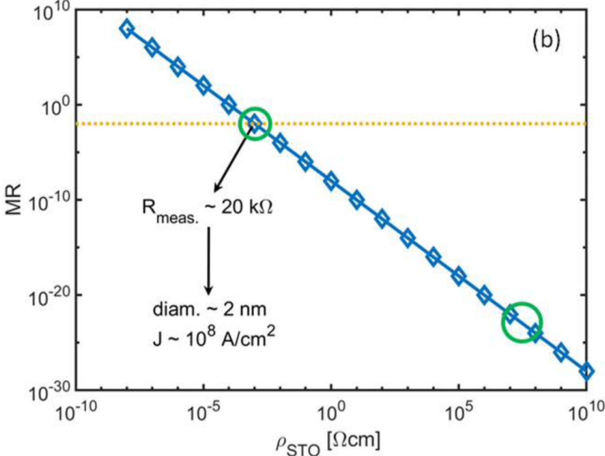

FIG. 8. (a) Electric field module $|\mathbf{F}|$ around a 2+ point charge vs the distance r from the charge, Eq. (8), assuming difference screening length and dielectric constant values, as in the legend. The red line corresponds to the programming field F_p. (b) Magnetoresistance (MR) as from Eq. (9), computed in terms of resistivities; we set the ratio between the spin mean free path in the LSMO and the transport distance d to unity and assume $r_{\mathrm{LSMO}} = 1\ \mathrm{m}\Omega\,\mathrm{cm}$. The green circles highlight the hypothetical measurement points discussed in the text for the case of homogeneous transport, bottom right circle, undetectable MR $\sim 10^{-24}$, and for the case of a matching resistivity, middle left circle, unrealistic current density. The yellow dotted line is our measured MR in Fig. 5(a).

believe we have channels with a very high carrier density embedded in a very low carrier density matrix. These high carrier density regions likely correspond to the regions of metallic transport reported in single-crystal STO [10], as we elucidate in the next section.

B. Spin transport

The investigation of spin transport allows us to add further knowledge about the transport properties in bad-metal STO, which we would not access by charge transport experiment only. We will see that the detection of the MR is very indicative and shows that we must consider transport terms and regimes additional to those described above. Indeed, to detect a measurable MR, it is necessary to overcome the well-known *conductivity mismatch* condition [58], accounting for the efficiency of the spin-polarized injection in the case of the diffusive transport regime.

Thus, accurate and straightforward considerations of the characteristic lengths and resistances involved in transport equations give for MR the following condition [58]:

$$\Delta R/R_P \sim \lambda_{\mathrm{FM}}/d(\sigma_{\mathrm{STO}}/\sigma_{\mathrm{LSMO}})^2, \tag{9}$$

where λ_{FM} is the spin-flip length in the ferromagnet, d is the thickness of the spin transport layer, and σ_{STO} and σ_{LSMO} are the conductivities of the transport layer and the ferromagnetic electrode correspondingly; ΔR is the difference in the resistance values between the parallel and antiparallel states, and R_P is the resistance in the parallel state. The conductivities are labeled according to our materials, and the choice of LSMO instead of Co is motivated by its lower conductivity (see below). The spin-flip length in ferromagnetic materials typically does not exceed 10 nm, so that the term $(\lambda_{\mathrm{FM}}/d)$ can be roughly set to 1.

Let us consider now various transport geometries and calculate corresponding σ_{STO} able to provide resistance values like those detected in our measurements. For a homogeneous transport across the whole contact area ($0.25\ \mathrm{mm}^2$), the resistivity of the 15-nm-thick STO layer would be some $10^7\ \Omega\,\mathrm{cm}$. Setting $(\lambda_{\mathrm{FM}}/d) = 1$ in Eq. (9) and taking the resistivity of the manganite electrode as $10^{-4}\ \Omega\,\mathrm{cm}$ estimates a vanishing MR value between 5×10^{-24} and 10^{-23}, i.e., deeply below any detection possibility, represented by a green circle in Fig. 8(b). Going to a more favorable [for Eq. (9)] situation and considering a conductive channel confined in only $1\ \mu\mathrm{m}^2$, a realistic macroscopic electroformed conductive path in the STO barrier [26], we obtain an estimate of MR $\Delta R/R \sim 10^{-12}$ that is again basically undetectable.

For the last estimation, we assume an STO resistivity able to offer the detected MR, dotted yellow line in Fig. 8(b). From the measured resistances and the device thickness, we obtain a transport section of $\sim 7\ \mathrm{nm}^2$ which results in a current density $\sim 10^8\ \mathrm{A/cm}^2$, which is unrealistic.

These considerations demonstrate that, for realistic conditions, the conductivity mismatch prevents the detection of any MR. Hence, its unequivocal presence in our devices, Fig. 5, is a strong indication that a homogeneously doped STO region, either involving the whole device area or even being constrained in a small part of it (10^{-5} for 1 μm channel), does not account for real microscopic pathways in STO.

Additional terms must be included thus in the overall picture of the charge transport in doped STO, undetectable from simple $R(T)$ measurements but clearly elucidated by the analysis of MR. Notoriously, adding in series tunneling resistive components would strongly support the development of MR [59–61], while leaving unmodified the general trend of the $R(T)$ dependencies. Thus, the highly doped STO regions described above do not connect the two ferromagnetic electrodes directly but through a tunneling resistance. Below, we

show that the realization of an interfacial barrier of Schottky type between Co and STO is fully realistic and that it can feature resistance values necessary for the detection of spin-polarized injection.

Let us assume for sake of simplicity that a heavily doped region of STO, doped with oxygen vacancies that migrated through the interface, is in contact with the electrode. If a Schottky contact is established, it will form a depletion region at the interface. Because both cobalt and LSMO have very similar work functions ~5 eV [23] and the electron affinity of STO can be estimated ~3.9 eV [62], we consider a built-in bias of 1 eV. In what follows, we use c.g.s. units. The potential inside the depletion layer can be described by [63]

$$V(z) = \frac{2\pi e^2 n}{\varepsilon}(z-L)^2. \tag{10}$$

In Eq. (10), $L = \sqrt{\frac{\varepsilon\phi}{2\pi e^2 n}}$, ε is the dielectric constant, ϕ the built-in potential, e the electron charge, and n the carrier density. We can estimate the tunneling transparency $\mathcal{T}$ of the depletion layer as [64]

$$\begin{aligned}\mathcal{T} &= \exp\left[-\frac{2}{\hbar}\int_0^L \sqrt{2mV(z)}dz\right] = \exp\left(-\frac{\phi}{\hbar}\sqrt{\frac{m\varepsilon}{\pi e^2 n}}\right)\\ &= \exp\left[-(\ln^{1/3})^2\sqrt{4\pi r_s\left(\frac{4\pi}{3}\right)^{1/3}}\right]\\ &\cong \exp[-4.5(\ln^{1/3})^2\sqrt{r_s}], \end{aligned} \tag{11}$$

where we introduced the dimensionless Wigner-Seitz radius $r_s = \frac{me^2}{\varepsilon\hbar}(\frac{3}{4\pi n})^{1/3}$.

Since we do not have any evidence of a Wigner crystal in the system, we must have $1 < r_s < 30$. To link $\mathcal{T}$ to a measurable resistance R, we adopt the following formula:

$$R = \frac{1}{N}\frac{R_Q}{\mathcal{T}}, \tag{12}$$

where $R_Q = 2\pi\hbar/e^2$ is the quantum resistance of a ballistic channel, and N is the number of conducting channels.

If we take the carrier density estimated above, $n = 10^{21}$ cm^{-3}, we obtain $\ln^{1/3} \sim 1.5$ and, from Eq. (11), for $r_s = 1$, $\mathcal{T} = 4.5 \times 10^{-5}$, respectively. These provide single channel resistances of $\sim 6.25 \times 10^8$ Ω. Therefore, for resistances of the order of 100 K Ω allowing us to circumvent the conductivity mismatch restrictions, a realistic number below several thousand metallic channels (filaments) needs to be formed per 0.25 mm^2.

Before concluding, it is worth mentioning that a very recent result on magnetotransport across a grain boundary in oxygen-vacancy-doped metallic STO corroborates our findings [65]. A ferromagnetic phase was observed, extended up to 300 K, likely related to the environment of Ti ions [66]. However, this reflects in the magnetotransport properties only <20 K and does not appear to be involved in our experiments. Additionally, a parabolic fit of their MR returns an intrinsic MR ~0.001 % at 0.3 T, which boosts the interpretation that our measured MR is related to the magnetization of the electrodes, i.e., to spin injection, transport, and detection across the device.

V. CONCLUSIONS

We demonstrate the possibility to establish spin-polarized injection and transport in bad-metal materials, namely, in oxygen-vacancy-doped STO thin films. The doping is performed by electromigration of oxygen atoms in vertical crossbar devices, involving two spin-polarized electrodes: LSMO manganite and Co. At low temperatures, the doped STO is metallic and behaves qualitatively and quantitatively very similarly to thermodynamically doped samples, while close to room temperature, the samples undergo MIT. We believe this transition reflects the filamentary nature of the transport across STO, a behavior typically created by electromigration, with a domination of highly doped metallic filaments at low temperatures and of insulating filaments and higher T. Additionally, we offered a robust approach to analyze the transport data in bad metals and to extract their significant parameters. We estimate that the electromigration process is a feasible way to achieve metallic doping concentrations as high as 10^{21} cm^{-3} capable of sustaining spin transport in bad metals. We believe our findings encourage promotion of doped STO and more generally bad metals as emerging materials for spintronic devices and applications.

The data supporting our findings here are available within this paper. The complete set of raw data supporting the findings of this paper are available from the corresponding authors upon reasonable request. The code used to analyze the data is available open source in the Supplemental Material [67].

ACKNOWLEDGMENTS

We have received funding from the European Community's H2020 Programme under Grant Agreement No. INTERFAST (H2020-FET-OPEN-965046), and from the European Community's Seventh Framework Programme (FP7/2007-2013) under Grant Agreement No. IFOX NMP3-LA-2010-246102 and COST Action MOLSPIN 15128. P.G. acknowledges financial support from Italian MIUR through PRIN project Project QCNaMos - 2015HYFSRT_005. We thank ELETTRA synchrotrons for the provision of synchrotron radiation facilities at beamline APE and Federico Bona (CNR) for technical support.

The authors declare no competing financial or nonfinancial interests.

L.V. and V.A.D. planned the experiment. P.G. conceived and conducted the analysis of transport and magnetotransport data and accomplished the theoretical analysis of the charge transport. P.G. and F.G. fabricated the devices. L.V., M.C., and A.R. performed the transport and magnetotransport measurements. D.A.McL. and K.J.O'S. performed the electron micrsoscopy measurements. I.B., F.B., G.V., P.T., and G.P. performed the spectroscopic characterization. V.K. accomplished the theoretical analysis of the spin transport. V.A.D. supervised the whole activity. P.G., I.B., and V.A.D. wrote the paper; all authors checked it.

[1] Y. Tokura, M. Kawasaki, and N. Nagaosa, Emergent functions of quantum materials, Nat. Phys. **13**, 1056 (2017).
[2] B. Keimer and J. E. Moore, The physics of quantum materials, Nat. Phys. **13**, 1045 (2017).
[3] C. Ahn, A. Cavalleri, A. Georges, S. Ismail-Beigi, A. J. Millis, and J.-M. Triscone, Designing and controlling the properties of transition metal oxide quantum materials, Nat. Mater. **20**, 1462 (2021).
[4] V. J. Emery and S. A. Kivelson, Superconductivity in Bad Metals, Phys. Rev. Lett. **74**, 3253 (1995).
[5] X. Deng, J. Mravlje, R. Žitko, M. Ferrero, G. Kotliar, and A. Georges, How Bad Metals Turn Good: Spectroscopic Signatures of Resilient Quasiparticles, Phys. Rev. Lett. **110**, 086401 (2013).
[6] L. de' Medici, G. Giovannetti, and M. Capone, Selective Mott Physics as a Key to Iron Superconductors, Phys. Rev. Lett. **112**, 177001 (2014).
[7] L. Fanfarillo, A. Valli, and M. Capone, Synergy between Hund-Driven Correlations and Boson-Mediated Superconductivity, Phys. Rev. Lett. **125**, 177001 (2020).
[8] S. A. Hartnoll, Theory of universal incoherent metallic transport, Nat. Phys. **11**, 54 (2015).
[9] N. Pakhira and R. H. McKenzie, Absence of a quantum limit to charge diffusion in bad metals, Phys. Rev. B **91**, 075124 (2015).
[10] X. Lin, C. W. Rischau, L. Buchauer, A. Jaoui, B. Fauqué, and K. Behnia, Metallicity without quasi-particles in room-temperature strontium titanate, npj Quantum Mater. **2**, 41 (2017).
[11] A. W. Tyler, A. P. Mackenzie, S. NishiZaki, and Y. Maeno, High-temperature resistivity of Sr_2RuO_4: Bad metallic transport in a good metal, Phys. Rev. B **58**, 10107(R) (1998).
[12] D.-Y. Cho, M. Luebben, S. Wiefels, K.-S. Lee, and I. Valov, Interfacial metal-oxide interactions in resistive switching memories, ACS Appl. Mater. Interfaces **9**, 19287 (2017).
[13] X. Lin, B. Fauqué, and K. Behnia, Scalable T^2 resistivity in a small single-component fermi surface, Science **349**, 945 (2015).
[14] D. van der Marel, J. L. M. van Mechelen, and I. I. Mazin, Common fermi-liquid origin of T^2 resistivity and superconductivity in *n*-type $SrTiO_3$, Phys. Rev. B **84**, 205111 (2011).
[15] A. Spinelli, M. A. Torija, C. Liu, C. Jan, and C. Leighton, Electronic transport in doped $SrTiO_3$: Conduction mechanisms and potential applications, Phys. Rev. B **81**, 155110 (2010).
[16] M.-J. Jin, D.-S. Um, K. Ohnishi, S. Komori, N. Stelmashenko, D. Choe, J.-W. Yoo, and J. W. A. Robinson, Pure spin currents driven by colossal spin-orbit coupling on two-dimensional surface conducting $SrTiO_3$, Nano Lett. **21**, 6511 (2021).
[17] A. Kandazoglou, C. Grezes, M. Cosset-Chéneau, L. M. Vincente-Arche, P. Sgarro, P. Noël, S. Auffret, K. Garello, M. Bibes, L. Vila *et al.*, Non-volatile electric-field control of spin-orbit torques in perpendicular ferromagnet-$SrTiO_3$ system (conference presentation), Proc. SPIE **PC12205**, PC122051E (2022).
[18] A. P. Mackenzie, J. W. Reiner, A. W. Tyler, L. M. Galvin, S. R. Julian, M. R. Beasley, T. H. Geballe, and A. Kapitulnik, Observation of quantum oscillations in the electrical resistivity of $SrRuO_3$, Phys. Rev. B **58**, R13318 (1998).
[19] S. Shimizu, K. S. Takahashi, M. Kubota, M. Kawasaki, Y. Tokura, and Y. Iwasa, Gate tuning of anomalous Hall effect in ferromagnetic metal $SrRuO_3$, Appl. Phys. Lett. **105**, 163509 (2014).
[20] S. Kamboj, D. K. Roy, S. Roy, R. R. Chowdhury, P. Mandal, M. Kabir, and G. Sheet, Temperature dependent transport spin-polarization in the low curie temperature complex itinerant ferromagnet $EuTi_{1-x}Nb_xO_3$, J. Phys. Condens. Matter **31**, 415601 (2019).
[21] J. M. De Teresa, A. Barthélémy, A. Fert, J. P. Contour, R. Lyonnet, F. Montaigne, P. Seneor, and A. Vaurès, Inverse Tunnel Magnetoresistance in $Co/SrTiO_3/La_{0.7}Sr_{0.3}MnO_3$: New Ideas on Spin-Polarized Tunneling, Phys. Rev. Lett. **82**, 4288 (1999).
[22] M. Bowen, J.-L. Maurice, A. Barthélémy, P. Prod'homme, E. Jacquet, J.-P. Contour, D. Imhoff, and C. Colliex, Bias-crafted magnetic tunnel junctions with bistable spin-dependent states, Appl. Phys. Lett. **89**, 103517 (2006).
[23] V. Dediu, L. E. Hueso, I. Bergenti, A. Riminucci, F. Borgatti, P. Graziosi, C. Newby, F. Casoli, M. P. De Jong, C. Taliani *et al.*, Room-temperature spintronic effects in Alq_3-based hybrid devices, Phys. Rev. B **78**, 115203 (2008).
[24] P. Graziosi, M. Prezioso, A. Gambardella, C. Kitts, R. K. Rakshit, A. Riminucci, I. Bergenti, F. Borgatti, C. Pernechele, M. Solzi *et al.*, Conditions for the growth of smooth $La_{0.7}Sr_{0.3}MnO_3$ thin films by pulsed electron ablation, Thin. Solid. Films **534**, 83 (2013).
[25] V. A. Dediu, J. López, F. C. Matacotta, P. Nozar, G. Ruani, R. Zamboni, and C. Taliani, Micro-Raman and resistance measurements of epitaxial $La_{0.7}Sr_{0.3}MnO_3$ films, Phys. Status Solidi B **215**, 625 (1999).
[26] H. Nili, S. Walia, S. Balendhran, D. B. Strukov, M. Bhaskaran, and S. Sriram, Nanoscale resistive switching in amorphous perovskite oxide (*a*-$SrTiO_3$) memristors, Adv. Funct. Mater. **24**, 6741 (2014).
[27] G. Panaccione, I. Vobornik, J. Fujii, D. Krizmancic, E. Annese, L. Giovanelli, F. Maccherozzi, F. Salvador, A. De Luisa, D. Benedetti *et al.*, Advanced photoelectric effect experiment beamline at Elettra: A surface science laboratory coupled with synchrotron radiation, Rev. Sci. Instrum. **80**, 043105 (2009).
[28] F. Motti, G. Vinai, A. Petrov, B. A. Davidson, B. Gobaut, A. Filippetti, G. Rossi, G. Panaccione, and P. Torelli, Strain-induced magnetization control in an oxide multiferroic heterostructure, Phys. Rev. B **97**, 094423 (2018).
[29] F. M. F. de Groot, J. C. Fuggle, B. T. Thole, and G. A. Sawatzky, $L_{2,3}$ x-ray-absorption edges of d^0 compounds: K^+, Ca^{2+}, Sc^{3+}, Ti^{4+} in O_h (octahedral) symmetry, Phys. Rev. B **41**, 928 (1990).
[30] G. van der Laan, Polaronic satellites in x-ray-absorption spectra, Phys. Rev. B **41**, 12366 (1990).
[31] G. Zhu, G. Radtke, and G. A. Botton, Bonding and structure of a reconstructed (001) surface of $SrTiO_3$ from TEM, Nature (London) **490**, 384 (2012).
[32] R. Laskowski and P. Blaha, Understanding the $L_{2,3}$ x-ray absorption spectra of early 3*d* transition elements, Phys. Rev. B **82**, 205104 (2010).
[33] L. C. Walters and R. E. Grace, Diffusion of point defects in strontium titanate, J. Phys. Chem. Solids **28**, 245 (1967).
[34] D. J. Keeble, Z. Li, and M. Harmatz, Electron paramagnetic resonance of Cu^{2+} in $PbTiO_3$, J. Phys. Chem. Solids **57**, 1513 (1996).
[35] M. S. Islam, Ionic transport in ABO_3 perovskite oxides: A computer modelling tour, J. Mater. Chem. **10**, 1027 (2000).

[36] R. Waser, R. Dittmann, G. Staikov, and K. Szot, Redox-based resistive switching memories—Nanoionic mechanisms, prospects, and challenges, Adv. Mater. **21**, 2632 (2009).
[37] D. B. Strukov and R. S. Williams, Exponential ionic drift: Fast switching and low volatility of thin-film memristors, Appl. Phys. A **94**, 515 (2009).
[38] I. Bergenti, T. Kamiya, D. Li, A. Riminucci, P. Graziosi, D. A. MacLaren, R. K. Rakshit, M. Singh, M. Benini, H. Tada *et al.*, Spinterface effects in hybrid $La_{0.7}Sr_{0.3}MnO_3/SrTiO_3/C_{60}/Co$ magnetic tunnel junctions, ACS Appl. Electron. Mater. (2022).
[39] R. Waser and M. Aono, Nanoionics-based resistive switching memories, Nat. Mater. **6**, 833 (2007).
[40] C. Collignon, P. Bourges, B. Fauqué, and K. Behnia, Heavy Nondegenerate Electrons in Doped Strontium Titanate, Phys. Rev. X **10**, 031025 (2020).
[41] A. S. Alexandrov and V. V. Kabanov, Unconventional High-Temperature Superconductivity from Repulsive Interactions: Theoretical Constraints, Phys. Rev. Lett. **106**, 136403 (2011).
[42] M. Egilmez, K. H. Chow, and J. Jung, Percolative model of the effect of disorder on the resistive peak broadening in $La_{2/3}Ca_{1/3}MnO_3$ near the metal-insulator transition, Appl. Phys. Lett. **92**, 162515 (2008).
[43] P. Graziosi, A. Gambardella, M. Prezioso, A. Riminucci, I. Bergenti, N. Homonnay, G. Schmidt, D. Pullini, and D. Busquets-Mataix, Polaron framework to account for transport properties in metallic epitaxial manganite films, Phys. Rev. B **89**, 214411 (2014).
[44] J. M. De Teresa, A. Barthélémy, A. Fert, J. P. Contour, F. Montaigne, and P. Seneor, Role of metal-oxide interface in determining the spin polarization of magnetic tunnel junctions, Science **286**, 507 (1999).
[45] I. I. Oleynik and E. Y. Tsymbal, Metal-oxide interfaces in magnetic tunnel junctions, Interface Sci. **12**, 105 (2004).
[46] K. Bairagi, A. Bellec, V. Repain, C. Chacon, Y. Girard, Y. Garreau, J. Lagoute, S. Rousset, R. Breitwieser, Y.-C. Hu *et al.*, Tuning the Magnetic Anisotropy at a Molecule-Metal Interface, Phys. Rev. Lett. **114**, 247203 (2015).
[47] K. V. Raman, N. Atodiresei, and J. S. Moodera, Tailoring Ferromagnet-Molecule Interfaces: Towards Molecular Spintronics, SPIN **4**, 1440014 (2014).
[48] M. Cinchetti, V. A. Dediu, and L. E. Hueso, Activating the molecular spinterface, Nat. Mater. **16**, 507 (2017).
[49] E. Y. Tsymbal, O. N. Mryasov, and P. R. LeClair, Spin-dependent tunnelling in magnetic tunnel junctions, J. Phys. Condens. Matter **15**, R109 (2003).
[50] A. Riminucci, M. Prezioso, P. Graziosi, and C. Newby, Electrode artifacts in low resistance organic spin valves, Appl. Phys. Lett. **96**, 112505 (2010).
[51] A. Hamza, Solving trascendental equations, proper setting, https://uk.mathworks.com/matlabcentral/answers/547923-solving-trascendental-equations-proper-setting?s_tid=mlc_ans_email_view#comment_897555.
[52] B. R. Nag, *Electron Transport in Compound Semiconductors* (Springer, Berlin, 1980), Vol. 11.
[53] J. M. Ziman, *Principles of the Theory of Solids*, 2nd edition (Cambridge University Press, Cambridge, 1979).
[54] S. Hong, S. M. Nakhmanson, and D. D. Fong, Screening mechanisms at polar oxide heterointerfaces, Rep. Prog. Phys. **79**, 076501 (2016).
[55] C. W. Rischau, X. Lin, C. P. Grams, D. Finck, S. Harms, J. Engelmayer, T. Lorenz, Y. Gallais, B. Fauqué, J. Hemberger *et al.*, A Ferroelectric quantum phase transition inside the superconducting dome of $Sr_{1-x}Ca_xTiO_{3-\delta}$, Nat. Phys. **13**, 643 (2017).
[56] J. Wang, L. Yang, C. W. Rischau, Z. Xu, Z. Ren, T. Lorenz, J. Hemberger, X. Lin, and K. Behnia, Charge transport in a polar metal, npj Quantum Mater. **4**, 61 (2019).
[57] Y. Huang, Y. Ayino, and B. I. Shklovskii, Metal-insulator transition in n-type bulk crystals and films of strongly compensated $SrTiO_3$, Phys. Rev. Mater. **5**, 044606 (2021).
[58] G. Schmidt, D. Ferrand, L. W. Molenkamp, A. T. Filip, and B. J. van Wees, Fundamental obstacle for electrical spin injection from a ferromagnetic metal into a diffusive semiconductor, Phys. Rev. B **62**, R4790 (2000).
[59] E. I. Rashba, Theory of electrical spin injection: Tunnel contacts as a solution of the conductivity mismatch problem, Phys. Rev. B **62**, R16267 (2000).
[60] A. Fert, J.-M. George, H. Jaffres, and R. Mattana, Semiconductors between spin-polarized sources and drains, IEEE Trans. Electron Devices **54**, 921 (2007).
[61] B. T. Jonker, Y. D. Park, B. R. Bennett, H. D. Cheong, G. Kioseoglou, and A. Petrou, Robust electrical spin injection into a semiconductor heterostructure, Phys. Rev. B **62**, 8180 (2000).
[62] J. Robertson and C. W. Chen, Schottky barrier heights of tantalum oxide, barium strontium titanate, lead titanate, and strontium bismuth tantalate, Appl. Phys. Lett. **74**, 1168 (1999).
[63] G. E. Pikus, *Fundamentals of the Theory of Semiconductor Devices* (Nauka, Moscow, 1965).
[64] L. D. Landau and E. M. Lifshitz, *Quantum Mechanics* (Pergamon, Oxford, 1977).
[65] M. Egilmez, S. El-Khatib, F. Mustafa, S. Ahmad, A. Di Bernardo, and J. W. A. Robinson, Concurrent weak localization and double Schottky barrier across a grain boundary in bicrystal $SrTiO_3$, Phys. Rev. B **107**, 104401 (2023).
[66] W. D. Rice, P. Ambwani, M. Bombeck, J. D. Thompson, G. Haugstad, C. Leighton, and S. A. Crooker, Persistent optically induced magnetism in oxygen-deficient strontium titanate, Nat. Mater. **13**, 481 (2014).
[67] See Supplemental Material at http://link.aps.org/supplemental/10.1103/PhysRevResearch.5.033096 for the code used to numerically solve Eq. (6).